Building and Environment 257 (2024) 111526

Contents lists available at ScienceDirect

Building and Environment

journal homepage: www.elsevier.com/locate/buildenv

CFD methodology for predicting thermal plume from heat source: Experimental validation and simplified model

Rafaela Mateus [a,b,*], Armando Pinto [b], José M.C. Pereira [a]

[a] LAETA, IDMEC, Instituto Superior Técnico, Universidade de Lisboa, Mechanical Engineering Department/LASEF, Av.Rovisco Pais, 1, Lisbon, 1049-001, Portugal
[b] NAICI, Laboratório Nacional de Engenharia Civil, Buildings Department, Av. Do Brasil 101, 1700-075, Lisboa, Portugal

ARTICLE INFO

Keywords:
Thermal plume
Heat sources
CFD methodology
Simplified model
Large air masses

ABSTRACT

The prediction of heat transfer in natural convection is crucial for various engineering applications, including building heating and natural ventilation. CFD study of heat transfer in elements with complex geometries, like radiators, increase the computational effort and could turn inviable the study of natural ventilation in large rooms with heating radiators. This study aimed to develop a CFD methodology and validate a simplified model to study natural convection and plumes above heat sources like heating radiators. The model uses porous media to simulate heat sources without compromising thermal plume development in large spaces. It enables cost-effective exploration of solutions, reducing computational costs while accurately modelling thermal plume effects. The CFD model was validated using a full-scale model experimental, ensuring its accuracy and reliability. The experimental measurements showed consistent evolutions for inlet and outlet water temperatures, indicating stable heat transfer processes. The study includes 5 heating scenarios in which the inlet and outlet water temperature (T_i/T_o) is varied, namely: 64/58 °C, 67/41 °C, 73/68 °C, 50/35 °C, and 39/29 °C. With the experiments and the CFD results, it was also concluded that the air temperature and velocity profiles in radiators configured in parallel are asymmetrical. The CFD simulations with the simplified model incorporating a porous medium demonstrated the effectiveness of the proposed methodology. Notably, the computational time for the simplified model was reduced by approximately 70 % compared to the detailed model. The developed CFD methodology has potential applications in optimizing natural ventilation systems for different radiators and environmental conditions, contributing to energy efficiency and occupant comfort.

1. Introduction

The prediction of heat transfer in natural convection is of great interest in different areas of engineering, particularly in the heating and ventilation of buildings, and in heat exchangers [1]. In the field of natural ventilation, developments have been carried out over the decades [2,3], since it plays a fundamental role in the energy performance and indoor air quality (IAQ) of existing buildings and Nearly Zero Energy Buildings (NZEB).

Energy efficiency is vital for reducing greenhouse gas emissions and combating climate change, with buildings accounting for 30 % of global emissions, posing a challenge to meeting Paris Agreement goals. The World Green Building Council stresses achieving “net zero carbon” operation by 2050 to limit global warming to 2 °C [4]. The EU aims to cut emissions by 80–95 % by 2050 compared to 1990 levels [5], underscoring the importance of enhancing energy efficiency for sustainability.

Eurostat’s January 2020 data shows 6.9 % of the EU population faces high energy poverty rates [6], resulting from factors like low income, inadequate housing conditions, and high energy prices. Energy poverty leads to health issues, social exclusion, and limited job opportunities.

Insufficient heating can cause discomfort for occupants, negatively impacting their health and well-being. It can also lead to condensation issues due to inadequate ventilation [7,8]. The proper use of thermal radiators has the potential to address heating problems [9] without compromising energy efficiency goals.

In the field of heat exchangers and heat sources (e.g., thermal radiators) to promote convection, studies have also been developed with the aim of ensuring energy efficiency and proper air distribution. These studies mainly focus on providing and analysing ways to increase their

* Corresponding author. LAETA, IDMEC, Instituto Superior Técnico, Universidade de Lisboa, Mechanical Engineering Department/LASEF, Av.Rovisco Pais, 1, Lisbon, 1049-001, Portugal.
E-mail address: rafaela.mateus@tecnico.ulisboa.pt (R. Mateus).

https://doi.org/10.1016/j.buildenv.2024.111526
Received 6 October 2023; Received in revised form 20 February 2024; Accepted 10 April 2024
Available online 16 April 2024

thermal efficiency by studying mostly changes in the geometry of the radiator's convectors in order to increase the transfer surface [9–17]. Other factors, such as flow type, connection type, position, and radiation, are also considered, although to a lesser extent [18–24].

In different areas, studying phenomena associated with natural convection, such as the specific case of thermal plumes, is essential to harness their full potential. However, the internal flow development in spaces with heat exchangers and heat sources remains relatively underexplored in the literature [25–27].

Thermal plumes associated with convective motion originated from localized heat sources are induced by temperature driven flow from a local heat source, which will be vertical if there are no cross air flows [28,29]. As the plume rises, it loses its connection with the source that produced it [30], particularly when the plume develops inside a large container. The evolution of the plume layer in the early stages of its formation reveals certain nonlinear properties that have been explored through different numerical approaches and observed in some experiments [31]. These types of plumes are special cases of nonlinear flow systems where buoyancy is constantly provided, and their development can occur in unconfined spaces and confined geometries [31].

In unconfined spaces, early studies utilized similarity solutions to describe natural convective flows [32]. Concurrently, experimental studies were conducted to validate laminar plume theory [28]. Discoveries regarding thermal plumes above horizontal heat sources include Urakawa et al. [33] demonstrating oscillations perpendicular to the heater plane and along its direction, with stable sinusoidal waveform observed at specific heater lengths. Advancements in analysing thermal plumes on building façades have also been noted [34].

In confined spaces, the buoyant flow induced by plume presence fills the enclosure, sensitive to wall boundary conditions affecting thermal stratification from distant flow fields, leading to strong intermittency [31,35]. Analytical approaches are challenging due to confinement, prompting the use of numerical simulations or experiments [35], often employing small cell dimensions [36,37].

In literature, various studies explore topics such as the evolution of initial thermal plumes from small heating plates in water using near-infrared images [36], numerical analysis of natural convection coupled with radiation in a cubic cavity [38], addressing inverse natural convection problems through experimental data analysis [39], examining the effect of human thermal plume and ventilation interaction on bacterial particle diffusion [40], analysing natural convection of vertical isothermal parallel plate arrays using steady-state numerical analysis [41], studying the statistics of thermal plumes and dissipation rates in turbulent Rayleigh-Bénard convection [36], investigating 3-D plume buoyancy effects on natural convection from vertical isothermal plate arrays [42], and analysing thermal plumes to assist in defining a method for judging radiator overheating in compensation of window downdraft based on thermal image velocimetry [12].

While the studies previous provide valuable insights into the behaviour of thermal plumes, it is important to note that most of them are conducted on small-scale domains and in controlled environments. This can limit the generalizability of the findings to real-world situations, where the conditions are often more complex and varied. Additionally, there may be important differences in the behaviour of thermal plumes at different scales and in different environments. Therefore, while the existing studies provide a strong foundation for understanding thermal plumes, and in certain cases [43,44], they rely on theoretical models, it is important to continue exploring their behaviour in a range of different settings and at different scales.

A numerical modelling of studies in confined spaces with large masses of air [45] converges with the type of unconfined flow, which is less numerically investigated. This is due to the complexity of imposing appropriate boundary conditions at the limits of the computational domain, especially in the case of unstable flows, and the high computational effort and time. However, efforts in this field have focused only on imposing analytical solutions at the external boundary and proposing new external boundary conditions for a limited computational domain [28]. There have been limited studies where simplification models are proposed [46,47].

In essence, investigating thermal plumes in large spaces using numerical models presents significant computational challenges, primarily due to the intricate demands of modelling detailed heat sources and the limited availability of experimental validation data for full-scale models. To overcome these challenges, our primary objective is to develop a simplified CFD model of heating radiators that accurately predicts the heat transfer in radiators (between liquid, solid and gas) and the development of thermal plumes above the radiator in large, uncontrolled environments. This model seeks to simplify geometry of the radiator without compromising accuracy and is validated using experimental data from a full-scale model. The main challenge lies in accurately modelling the complex and often unpredictable behaviour of plumes in dynamic environments, requiring substantial computational power and careful selection of boundary conditions. The established CFD methodology holds potential for application to various radiator types and diverse environmental conditions.

Overall, our simplified model aims to streamline the numerical modelling process for new construction and the rehabilitation of large spaces with multiple heat sources, such as atriums, sports complexes, industrial pavilions, spas, and pools, enabling the study of various solutions. This approach facilitates the study and implementation of natural ventilation solutions without high and time-consuming computational costs, ensuring the modelling of the effects of thermal plumes.

2. Problem formulation

When utilizing vertical surface heat sources with hot water as the heat source, heat transfer occurs through the circulation of hot water within the hollow channels of the radiator's metallic elements. The heat transfer by forced convection takes place from the hot water to the hollow channels surfaces of the radiator's panels, subsequently conducting the heat through the metallic elements. The resulting heat is then conveyed to the surrounding air by natural convection and infrared radiation to nearby surfaces.

To calculate the heat transfer from hot water to the radiator, Equation (1) can be employed. This equation relies on the water enthalpies gap between the inlet and outlet sections, and the water flow rate passing through the radiators. The excess temperature of vertical surface heat sources above indoor air temperature was determined based on Equation (2) [48] and Equation (3) describes the heat transfer by natural convection, following Newton's law of cooling, from radiator surface to the air. The radiation heat transfer from the vertical surface heat source to the room surfaces can be determined by Equation (4) and Equation (5), respectively [49].

$$Q = \rho \dot{Q}(h_i - h_o) \tag{1}$$

Where ρ is the water density [kg/m^3], $\dot{Q}$ is the water flow rate [m^3/s], h_i and h_o are the water enthalpy [J/kg] at the inlet and outlet, respectively. The enthalpies were acquired by referring to thermodynamic tables [50].

$$\Delta T = \frac{T_i + T_o}{2} - T_r \tag{2}$$

Where T_r is the room air temperature, T_i and T_o are the inlet and outlet water temperatures, respectively [°C].

$$Q_{convection} = hA_{conv}(T_s - T_r) \tag{3}$$

Where $Q_{convection}$ is the convective heat rate transferred through the exposed surface of the vertical surface heat source [W], T_s is the average surface temperature of the vertical surface heat sources [°C], h is the average convective coefficient which is a function of the fluid flow or velocity, fluid thermal properties, physical geometry and direction of the surface [W/m^2 °C], and A is the total surface area of the vertical surface heat sources [m^2].

The average frontal surface temperature of a vertical surface heat source (T_s) was determined by calculating the average of a restricted number of temperatures measured. The local convection coefficient changes along the height of the vertical surface heat source and it is influenced by the specific location where the air temperature was being measured. Consequently, an average convection coefficient was employed.

$$Q_{radiation1} = A_{rad}\xi_{rad}\sigma\left(T_s^4 - T_r^4\right) \tag{4}$$

$$Q_{radiation2} = A_{rad}\xi_{rad-w}\sigma\left(T_s^4 - T_r^4\right) \text{ with } \xi_{rad-w} = \left(\frac{1}{\xi_{rad}} + \frac{1}{\xi_w} - 1\right)^{-1} \tag{5}$$

Where σ is the Stefan–Boltzmann constant (5.6703 × 10^8 W/m^2 K^4), A_{rad} is the radiator frontal surface area (m^2), ξ_{rad} is the radiator emissivity, ξ_{rad-w} is the radiator-back wall emissivity, and ξ_w is the emissivity of the wall.

3. Methodology

3.1. Experimental setup

The experimental setup of the vertical surface heat source heating system consisted of the following components: a water heater tank responsible for storing and heating water, a pump that circulates the heated water throughout the system, a flow meter to measure the water flow rate, a filling unit that facilitates easy refilling of the system, two radiators with 8 elements each, installed in a parallel configuration, insulated pipes to minimize heat loss (hot water circuit and return circuit), and associated accessories. For each radiator, the TBOE (Top and Bottom Opposite End) connection method was employed, allowing the water flow and return to be positioned at the top and bottom, respectively, at opposite ends of the vertical surface heat source. This arrangement ensured that the water passes through the entire radiator, maximizing its efficiency.

Fig. 1-a illustrates a schematic representation of the experimental installation, depicting the hot water circuit in red, the return circuit in blue, and the cold-water circuit in green. The vertical surface heat sources were installed 110 mm away from the wall to which they were fixed, 500 mm from the floor, with a distance of 1068 mm from the left side pillar, and 260 mm between the radiators, this installation was situated at LNEC, Lisbon-Portugal, within the testing space of the Component Test Building, operating under ambient conditions without controlled temperature and humidity. The testing space has a width of 14700 mm, a height of 10000 mm, and a length of 29000 mm. Within this space, there are multiple test segments, and this facility is situated between two columns, on a wall with a beam at a height of approximately 3500 mm.

The experimental setup employed vertical surface heat sources comprising diecast and extruded aluminium radiators with 8 elements in white color. The single element is characterized by the overall dimensions shown in Fig. 1-b, a hollow channel with a diameter of 12.7 mm, and a heat output for ΔT = 50 °C of 321 W, determined in accordance with the EN 442 standard [48].

3.1.1. Measurement's equipment

Thermocouples DS18B20 were used to measure the hot water inlet and outlet temperatures, while a humidity and temperature data logger was used to monitor the room temperature and relative humidity of the ambient conditions. The measurements were monitored by a Raspberry Pi and assisted by a Phyton program developed for signal data processing.

Thermo-anemometers equipped with hot wire probes were used to measure the air velocity and temperature above the radiators. In addition, a thermal camera (emissivity of 0.9) was used to determine the distribution on the radiators surface temperature (T_s).

Table 1 presents the specifications of each measuring equipment. The test conditions and the different measurement scenarios are presented in Section 3.1.2.

3.1.2. Test conditions and measurement scenarios

The measurements were carried out between February 7th and 16th, 2023. Each scenario (Table 2) was monitored for one day within the timeframe of 07:00 a.m. to 05:00 p.m. During each experimenting day, the pump operated under a constant flow rate, and the water heater was adjusted according to the specific scenario.

According to the number of available equipment and the objective of the study, air temperature and velocity were monitored in 3 vertical planes (V1–V3), 4 horizontal planes (H1–H4), and 7 longitudinal planes (L1-L7), respectively in the x, z, and y directions, as illustrated in Fig. 2.

The V1 to V3 planes are located at x = −102.5 mm, x = 0 mm, and x = 102.5 mm, respectively; and x = 0 is in the middle of the radiator and V1 and V3 are placed 55 mm beyond radiator surface. The H1 to H4 planes are located between z = 2023 mm and z = 2923 mm, spaced 180 mm apart. Lastly, the longitudinal planes were located halfway between the first and last element of each radiator and the L4 plane was located halfway between the two radiators (L1: y = 40 mm; L2: y = 320 mm; L3:

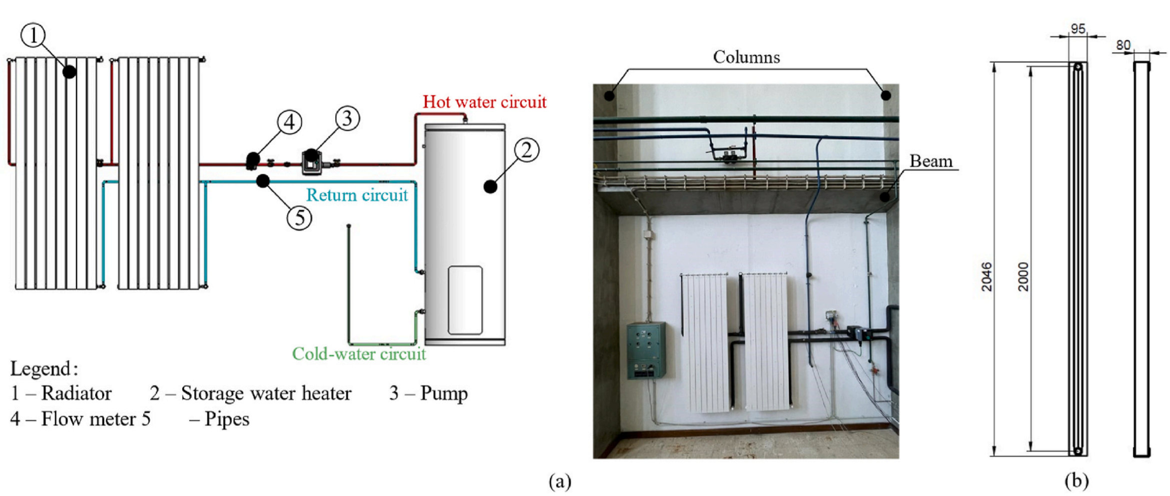

Fig. 1. Experimental installation: a) layout and b) 1 element of radiator.

Table 1
Specifications of measuring equipment.

Equipment		Range		Accuracy	Resolution
		Min	Max		
Humidity and temperature data logger	Humidity (%)	0	100	±1.5	0.01
	Temperature (°C)	−30	70	±0.2	0.01
Thermocouples DS18B20	Temperature (°C)	−55	125	±0.5	0.001
Thermo-anemometers (Van probe)	Velocity (m/s)	0.3	35	±(0.1 m/s + 1.5 % of mv[a]) (0.3–20 m/s) ±(0.2 m/s + 1.5 % of mv[a]) (20–35 m/s)	0.01
	Temperature (°C)	−20	70	±0.5	0.1
Thermal Camera	Temperature (°C)	0	350	–	0.1

[a] Mv corresponds to the measured value.

Table 2
Environment and operating conditions average of the 5 experimental measurement scenarios.

Variables	Scenarios (Inlet/Outlet Temperature)				
	64/58 °C	67/41 °C	73/68 °C	50/35 °C	39/29 °C
T_i (°C)	64.3	67.7	73.8	50.9	39.5
T_o (°C)	58.7	41.4	68.6	34.6	29.0
T_r (°C)	15.0	15.3	16.5	16.7	16.4
ΔT (°C)	46	39	55	26	18
$\dot{Q}$ (m^3/h)	0.90	0.12	1.20	0.11	0.10

y = 600 mm; L4; y = 770 mm; L5: y = 940 mm; L6: y = 1 220 mm; L7: y = 1 500 mm). The two radiators will be referred to as RAD1 and RAD2 from now on. The intersection of the vertical and longitudinal planes results in a total of 21 points, and measurements for the horizontal planes were conducted at each of these points, resulting in a total of 84 measurement points overall. For each point, data acquisition was performed continuously for 5 min with a sampling rate of 1 s. The inlet and outlet water temperature are monitored at a point in the piping shared by both radiators, with a sampling rate of 1 s.

In addition to these parameters, the front surface temperature of the radiators was evaluated at multiple points in three measurement cases (Case I to III) as illustrated in Fig. 3. Each point was subjected to three thermographic measurements to ensure accuracy and reliability and the measurements was taken at the center of the radiator elements. Case I involved four specific points on the radiator surface. In Case II, the evaluation expands to six points, capturing additional temperature data from various locations on the radiator surface. Finally, Case III included a comprehensive analysis with measurements taken at sixteen distinct points, providing a detailed understanding of the temperature distribution across the radiator surface.

The monitoring of all these parameters was carried out for 5 scenarios in which the inlet water temperature and pump flow rate were varied to cover the typical range of the excess temperature of vertical surface heat sources (ΔT), as presented in Table 2. The measurements for each scenario were carried out within a single day, amounting to a total of five days of testing. The scenarios were meticulously chosen to encompass the conditions outlined in the study of Pinto, 2018 [51], as this research is embedded within a larger macro-scale investigation of the Roman Baths in Chaves, Portugal. This strategic selection ensured that the experiments captured a comprehensive range of conditions relevant to the overarching study.

3.2. CFD methodology

To simulate the thermal plumes of the radiators, the STAR-CCM + software was utilized, which employs the finite volume method (FVM) to solve the fundamental equations governing fluid mechanics and heat transfer.

The CFD methodology, depicted in Fig. 4, encompasses two steps to obtain a validated operational model which requires low computation resources to assess heat transfer from water to the radiator and from radiator surface to the environment, namely natural convection buoyancy (plume) at induced by the heated radiator surfaces. The methodology relies on a simplified model suitable for studying large air volumes

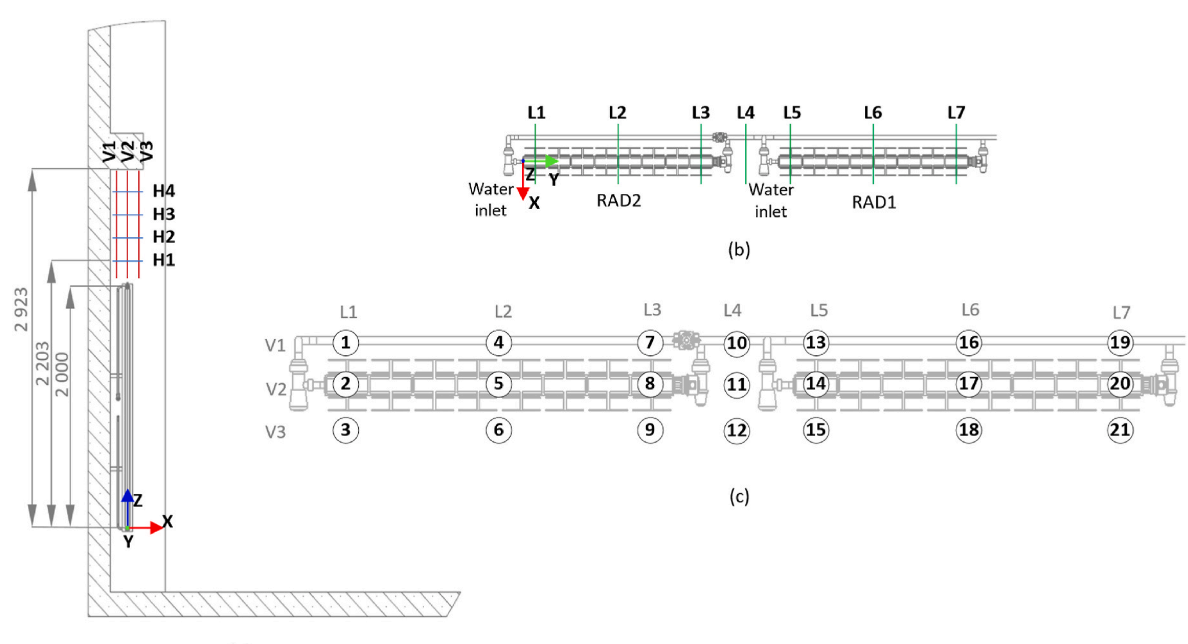

Fig. 2. Temperature and velocity measurement's locations: (a) above installation, (b) along length of two radiators (c) measured points in each plane H.

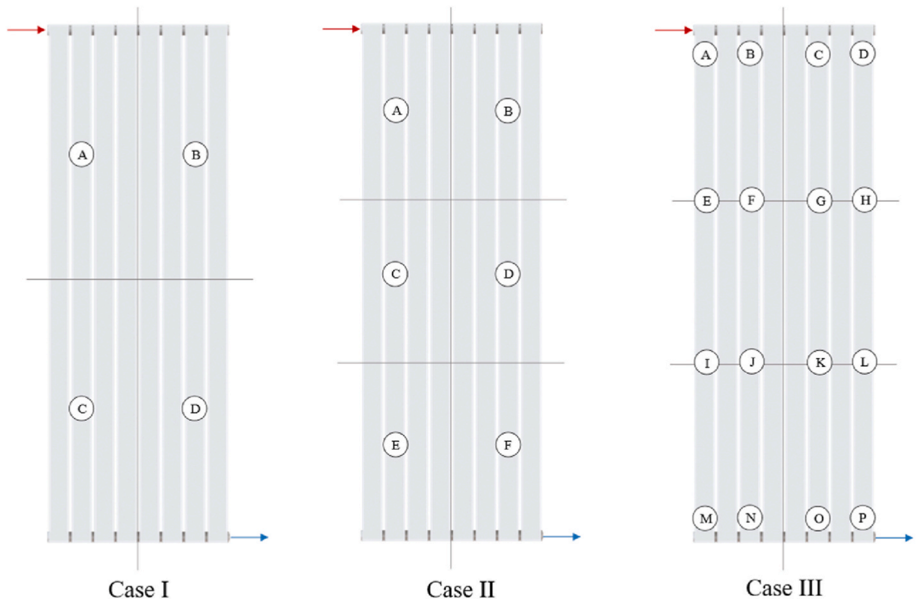

Fig. 3. Cases selected to evaluate the radiators' surface temperature.

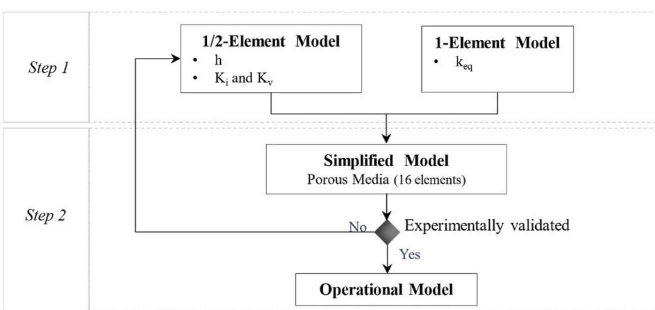

Fig. 4. CFD methodology.

without compromising the accurate prediction of thermal plumes.

Step 1 entails the creation of two parallel models. Firstly, a 1/2-Element Model of the radiator was developed, which includes all three regions (liquid, solid, and gas). To determine the convection coefficient (h) within the desired operational range, at least six simulations are performed. This coefficient can then be interpolated for all conditions within the specified range. Additionally, viscous, and inertial resistance coefficients (K_v and K_i) are derived, representing characteristics of the porous medium, as explained in detail in next section Secondly, a 1-Element Model of the radiator was created, which solely encompasses the solid region. This model undergoes a temperature variation to determine the equivalent conductivity of the material in each direction, which will be used in the simplified model (See Fig. 5).

In the Step 2, a Simplified Model was developed using a porous media (PM) approach to represent the 16 elements of the radiators. This model incorporates the properties determined in Step 1. The results obtained from this Simplified Model are then compared with both the numerical results from the Detailed Model and the experimental results. If the discrepancy between these results is less than 10 %, the process was considered complete, and the model was deemed operational for conducting sensitivity studies and developing more effective strategies for managing and controlling plumes in spaces with large masses of air and without controlled environmental conditions. Complementarily, for a detailed understanding of the geometric details and simplifications of each model at every step, refer to Fig. 5 in section 3.2.2.

In this study, a brief comparison is also made with a Detailed Model, where radiators were modelled with all their specificities (16 elements), in order to analyse the effectiveness of the simplified model and reinforce its potential for simulating spaces with large air masses.

3.2.1. Governing equations and models

The problem under investigation was solved using the governing equations for a three-dimensional, turbulent, and incompressible flow. Within the radiator's water channels, heat transfer occurs through forced convection as hot water circulates. The heat is then conducted through the radiator panels, ultimately heating the surrounding air in the environment. As a result, the density of air decreases, causing it to rise. The natural convection air flow was modelled using the Boussinesq approximation and the radiation heat loss is considered using the surface to surface (S2S) model. Furthermore, the study utilized unsteady-state models with a time step of 0.01 s, deeming the transient state approach more suitable for ensuring proper simulation convergence.

The equations of mass conservation (Equation (6)), linear momentum conservation (Equation (7)), and energy conservation in enthalpy form (Equation (8)) [52] were solved using the SIMPLE algorithm (Semi-Implicit Method for Pressure Linked Equations), where the mass and momentum equations were solved independently, and the pressure was corrected based on a predictive-corrective model. After discretizing the domain, these equations were solved by the software through integration over the control volume.

$$\frac{\partial \rho}{\partial t} + \nabla \bullet (\rho \mathbf{v}) = 0 \tag{6}$$

$$\frac{\partial (\rho \mathbf{v})}{\partial t} + \nabla \bullet (\rho \mathbf{v} \otimes \mathbf{v}) = \nabla \bullet \sigma + \mathbf{f_b} \tag{7}$$

$$\frac{\partial (\rho H)}{\partial t} + \nabla \bullet (\rho H \mathbf{v}) = \mathbf{f_b} \cdot \mathbf{v} + \nabla \bullet (\mathbf{v} \bullet \boldsymbol{\sigma}) - \nabla \bullet \mathbf{q} + S_E \tag{8}$$

Where ρ is the density, that is, the mass per unit volume, $\mathbf{v}$ is the continuum velocity, $\otimes$ denotes the outer product, $\mathbf{f_b}$ is the resultant of the body forces per unit volume acting on the continuum, σ is the stress tensor, H is the specific enthalpy, $\mathbf{q}$ is the heat flux, and S_E is an energy source per unit volume.

Turbulence effects were modelled using the Realizable k-ε Two-Layer turbulence model within the RANS framework. This model includes equations for turbulent kinetic energy and dissipation rate, assuming fully turbulent flow with negligible molecular viscosity effects. Turbulent viscosity is expressed proportionally to k squared and inversely

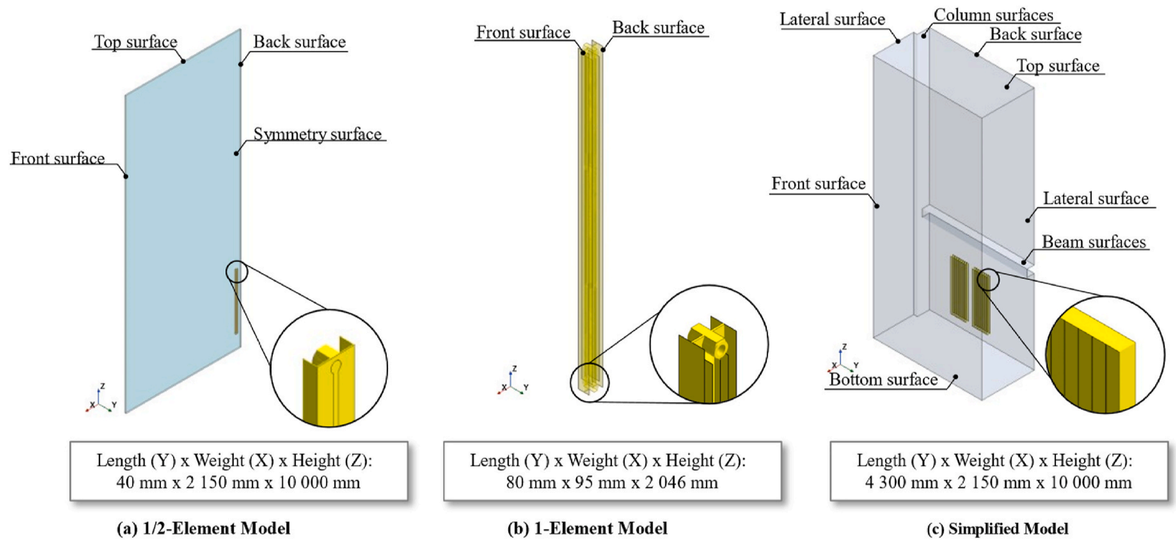

Fig. 5. Dimensions and geometrical details of the computational domains: a) 1/2-Element Model (Step a), b) 1-Element Model (Step 1) and c) Simplified Model (Step 2).

proportional to ε. Equations (9)–(11) detail these aspects [52]. The Realizable k-ε Two-Layer model shares equations with the Standard k-ε model but differs in wall treatment, employing an all-y$^+$ approach near the wall.

$$\mu_t = \frac{\rho C_\mu k^2}{\varepsilon} \tag{9}$$

$$\frac{\partial}{\partial t}(\rho k) + \nabla \bullet (\rho k \bar{\mathbf{v}}) = \nabla \bullet \left[\left(\mu + \frac{\mu_t}{\sigma_k} \right) \nabla k \right] + P_k - \rho(\varepsilon - \varepsilon_0) + S_k \tag{10}$$

$$\frac{\partial}{\partial t}(\rho \varepsilon) + \nabla \bullet (\rho \varepsilon \bar{\mathbf{v}}) = \nabla \bullet \left[\left(\mu + \frac{\mu_t}{\sigma_\varepsilon} \right) \nabla \varepsilon \right] + \frac{1}{T_e} C_{\varepsilon 1} P_\varepsilon - C_{\varepsilon 2} \rho \left(\frac{\varepsilon}{T_e} - \frac{\varepsilon_0}{T_0} \right) + S_\varepsilon \tag{11}$$

Where C_μ is a dimensionless constant, $\bar{\mathbf{v}}$ is the mean velocity, μ is the dynamic viscosity, σ_k, σ_ε, $C_{\varepsilon 1}$ and $C_{\varepsilon 2}$ are model constants, P_k and P_ε are production terms, $T_e = k/\varepsilon$ is the large-eddy time scale, ε_0 is the ambient turbulence value in the source terms that counteracts turbulence decay, T_0 is a specific time-scale, and S_k and S_ε are the user-specified source terms.

The simplification of the radiator's complex geometry was performed using a porous media (PM). A PM is defined as a solid that allows the passage of a fluid. In the simulation, the use of a PM allows governing the flow and heat transfer the replacement of the radiator by modifying the equations. This model was based on Darcy-Forchheimer's law, where two resistances can be distinguished: one of viscous nature (derived from the stresses generated due to friction on the walls) and another of inertial nature (derived from the flow profile) [53].

The porosity of the solid is characterized by Equation (12), and this parameter was crucial for solving the equations governing the flow and heat transfer in PM, respectively Equations (13) and (14) [52].

$$\chi = \frac{V_f}{V} \tag{12}$$

$$\frac{\partial \chi \rho}{\partial t} + \nabla \bullet (\rho \chi \mathbf{v}) = 0 \tag{13}$$

$$\frac{\partial \chi \rho \mathbf{v}}{\partial t} + \nabla \bullet (\rho \chi \mathrm{vv}) = -\chi \nabla \mathrm{p} + \nabla \bullet (\chi \mathbf{T}) - \chi \mathbf{P}_\mathrm{v} \mathbf{v}_\mathrm{s} - \chi \mathbf{P}_\mathrm{i} |\mathbf{v}_\mathrm{s}| \mathbf{v}_\mathrm{s} \tag{14}$$

Where V_f is the volume that is occupied by the fluid, V is the total volume, $\mathbf{v}$ is the fluid velocity, $\mathbf{T}$ is the stress tensor, $\mathbf{P}_\mathrm{v}$ and $\mathbf{P}_\mathrm{i}$ is the viscous and inertial resistance tensor, $\mathbf{v}_\mathrm{s}$ is the superficial velocity, $\mathbf{v}_\mathrm{s} = \chi\, \mathbf{v}$.

The software used provides two models for porous media energy: the equilibrium and the non-equilibrium model. The equilibrium energy model, also known as the thermal equilibrium model, assumes that the temperatures of fluids and solids in porous media are in equilibrium, making it suitable for fast thermal response times. In contrast, the non-equilibrium model treats fluid and solid temperatures as independent, allowing simulation of slower thermal responses and significant thermal imbalances.

In this study, the non-equilibrium model (Equations (15) and (16)) was chosen to be used as it enables a better representation of reality, allowing for a distinction between the two phases while maintaining their respective properties.

$$\frac{\partial \left(\chi \rho_{fluid} E_{fluid} \right)}{\partial t} + \nabla \bullet \left(\chi \rho_{fluid} H_{fluid} \mathbf{v} \right) = -\nabla \bullet \left(\chi \mathbf{q}_{fluid} \right) + \nabla \bullet (\chi \mathbf{T} \bullet \mathrm{v}) + A h_t \left(T_{fluid} - T_{solid} \right) \tag{15}$$

$$\frac{\partial ((1-\chi) \rho_{solid} E_{solid})}{\partial t} = -\nabla \bullet ((1-\chi) \mathbf{q}_{solid}) + A h_t \left(T_{solid} - T_{fluid} \right) \tag{16}$$

Where E_{fluid} is the total energy of the fluid, H_{fluid} is the total enthalpy of the fluid, $\mathbf{q}_{fluid}$ is the conduction heat flux through the fluid phase, A is the interaction area density ($A = A_{solid} / V_{solid}$) [54], h_t is the heat transfer coeficient, and $\mathbf{q}_{solid}$ conduction heat flux through the solid phase.

In summary, for the application of the porous media, it was necessary to know in advance the heat transfer coefficient h_t, the interaction area between both phases, A, the equivalent conductivity of the material, k_{eq}, the water temperature profile, and the resistance of the porous media ($\mathrm{P_v} = \mu / \mathrm{K_v}$, $\mathrm{P_i} = \rho / \mathrm{K_i}$).

The values of P_v and P_i can be obtained using experimental data or based on the numerical values obtained in Step 2 using the 1/2-Element Model, by determining the pressure drop per unit length of the porous media for various velocities. The various data points are then fitted to Equation (17). The resistance coefficients values depend on the flow direction with respect to the porous media. For porous media that are impermeable in a certain direction, STAR-CCM + [52] simulates the impermeability in a non-natural way by imposing a very high value to the inertial and viscous resistances.

$$\frac{\Delta P}{L} = \frac{\mu}{\mathrm{K_v}} \mathrm{v} + \frac{\rho}{\mathrm{K_i}} \mathrm{v} |\mathrm{v}| \tag{17}$$

When the radiator is modelled as a parallelepiped porous media, its original shape ceases to exist, and due to the change in geometry, a new thermal conductivity needs to be calculated, known as the equivalent conductivity. For radiators, the x-direction was preferred for heat flow, so the calculation of k_{eq} (Equation (18)) was performed only for this direction, while the original conductivity of the radiator material was applied in the other directions, as the porous media model allows for anisotropic conductivity of the solid phase. To determine k_{eq}, numerical data from Step 2 of the 1-Element Model were used.

$$k_{eq} = \frac{q_x}{HL\Delta T} \tag{18}$$

Where H is the height and L is the length of radiator.

To determine the heat transfer coefficient, the expression given in Equation (19) was used along with the simulation results from Step 1 using 1/2-Element Model in the CFD methodology.

$$h_t = \frac{q}{A_s LMTD} \; with \; LMTD = \frac{\left(T_s - T_{air,out}\right) - \left(T_s - T_{air,in}\right)}{ln\left(\frac{\left(T_s - T_{air,out}\right)}{\left(T_s - T_{air,in}\right)}\right)} \tag{19}$$

Where q is the heat flux rate, A_s is the surface contact area and LMTD is the Logarithmic Mean Temperature Difference.

Finally, as the objective is to apply the model to volumes with large air masses, simplifications are necessary to minimize the required physical models. In the case of the water circulating inside the radiator, these simplifications are reflected in a profile exhibiting linear behaviour. This profile is determined considering the expected design data for each installation, and if available, experimental data can also be applied, or determined based on information provided by the manufacturers of the heat sources. Therefore, the simplified temperature profile of the water, which varies in height (coordinate z), was derived from the inlet and outlet temperature, and expressed using Equation (20).

$$T(z) = \frac{T_i - T_o}{H} \bullet z + T_o \tag{20}$$

Where z is the vertical coordinate.

3.2.2. Computational domain and boundary conditions

The computational domain and geometric parameters for the models utilized in the two steps of the CFD methodology (section 3.2) are presented in Fig. 5-a showcases the 1/2-Element Model and Fig. 5-b demonstrate the 1-Element Model, which were employed simultaneously in Step 1. Lastly, Fig. 5-c exhibits the Simplified Model, incorporating the porous media. Each model provides a detailed representation of the radiator geometry.

The Simplified Model dimensions were based on the size of the testing room. However, lateral limitations (4300 mm) and frontal restrictions (2150 mm) were enforced due to the presence of other testing segments within the total volume, geometrically constraining the available area, particularly owing to the existence of isolated testing chambers. Considering these constraints, Table 3 outlines the specific boundary conditions applied in each simulation. Additionally, Table 4 provides a comprehensive overview of the material properties utilized in the CFD models, encompassing air, water, and aluminium, along with detailed specifications. Specifically, the lateral boundaries of the domain were considered as walls, given the presence of isolated testing chambers at the periphery of the columns constraining the radiator installation site. Frontally, a pressure outlet condition was applied to ensure flow propagation, given that the total room length is approximately 29000 mm while the model extends only up to 2150 mm. This reduction was implemented to optimize computational effort without compromising the development of the thermal plume, as observed mainly near the room's rear wall.

The coordinate system used in the simulations aligned with that in the experimental measurements (Fig. 2), featuring a gravitational force of 9.81 m/s^2 applied in the negative z direction. Emissivity values for the room walls and radiator panels were assigned as 0.91 and 0.95, respectively [55]. Similar to the experimental study, the connection pipes were insulated, making the panel radiator the sole heat source within the computational domain.

Regarding the mesh used for simulations in both stages of the methodology, an isotropic mesh with polyhedral elements was generated, defining control volumes to minimize the number of elements required for domain discretization. Mesh dependency study was initially conducted for the 1/2 Element Model and subsequently applied to a Detailed Model, which was then used as a basis for the Simplified Model. For the Detailed Model, only results from the finer mesh and the mesh where the parameters of outlet water temperature and heat production

Table 4
Thermal properties of materials used in CFD models [50,56].

	Gas	Solid	Liquid
Material	Air	Aluminum	Water
Density (kg/m^3)	1.18415	2730.0	977.7
Dynamic viscosity (Pa.s)	1.86E-5	–	0.0004
Specific Heat (J/(kg.K))	1003.6	893.0	4181.7
Thermal Conductivity (W/(m.K))	0.03	163.0	0.6

Table 3
Simulations characteristics and boundary conditions.

			1/2-Element Model	1-Element Model	Simplified Model
Radiator element	Detailed		1/2	1	–
	Simplified		–	–	16
Materials	Gas		x	–	x
	Solid		x	x	–
	Liquid		x	–	–
	Porous media		–	–	x
Boundary conditions	Gas	Front surface	Pressure outlet	–	Pressure outlet
		Lateral surfaces	Symmetric	–	Wall - Adiabatic
		Other surfaces	Wall - Adiabatic		
	Solid	Front and Back surfaces	Wall	Wall - Temperature	–
		Lateral surfaces	Symmetric	Wall - Adiabatic	
		Other surfaces	Wall		
	Liquid	Inlet	Mass Flow Inlet	–	
		Outlet	Outflow	–	
	Porous media	Volume	–		Porosity
					Interaction area K_v, K_i
Interfaces	Gas-Solid	All surfaces	Mapped contact	–	–
	Liquid-Solid	All surfaces			
	Gas-PM	Front and Back surfaces	–		Baffle
		Other surfaces			Internal

showed variation less than or equal to 1 % compared to the finer mesh are presented. This was done to identify the impact of mesh replication for a larger number of elements in sequence. The study of the 1/2-Element Model comprised four meshes with 0.3 M, 0.6 M, 1 M, and 2 M cells, referred to as Mesh 1 (coarser), Mesh 2, Mesh 3, and Mesh 4 (finer), with cell sizes in the radiator region corresponding to 7.5 mm, 5 mm, 3.5 mm, and 2.5 mm, respectively. The results showed that from Mesh2 onwards, the relative error for the outlet water temperature and the heat output of radiators was below 0.03 % and 1 %, respectively.

Creating two meshes with the characteristics of Mesh2 and Mesh4 in the case of the Detailed Model aimed to identify the impact of mesh replication for a larger number of elements in sequence and including two radiators. The results demonstrated that for the Detailed Model, comparing the outlet water temperature and the heat output of radiators using cells with 5 mm and 2.5 mm, one with 18 M cells and another with 58 M cells, the relative error between the two meshes was below 0.5 % for both parameters. The more refined mesh was considered the more accurate representation, and its values were used for calculating the relative error. Given the reduced relative error and lower computational time, the mesh with 18 M cells (Fig. 6) was used in the models. For the Simplified Models, the mesh parameters resulting from the mesh dependency study of the Detailed Model were applied. The mesh of the Detailed Model was characterized by approximately 18 M cells, while the mesh of the Simplified Model was characterized by only 3 M cells. Compared to the Detailed Model, there was a reduction of approximately 83 %, resulting from the use of porous media, which minimized geometric details.

4. Results and discussions

In this section, the experimental and CFD model results are presented, including variations in velocity and temperature for the 5 scenarios listed in Table 2. Finally, these results were compared to validate the model and the methodology used to create a simplified model of vertical heat sources, enabling the prediction of thermal plumes and their application to spaces with large air masses without significant computational efforts.

4.1. Experimental

For each scenario presented in Table 2, the room air temperature, inlet and outlet water temperatures evolutions of the radiators were determined. These evolutions are shown in Fig. 7 and correspond to the period between 07:00 and 17:00. The average ambient temperature was determined since the test location is not a controlled environment and will be used in the numerical simulation. For the five scenarios (T_i/T_o) 64/58 °C, 67/41 °C, 73/68 °C, 50/35 °C and 39/29 °C, an average ambient temperature of 15.03 °C, 15.31 °C, 16.50 °C, 16.71 °C, and 16.41 °C was recorded, respectively.

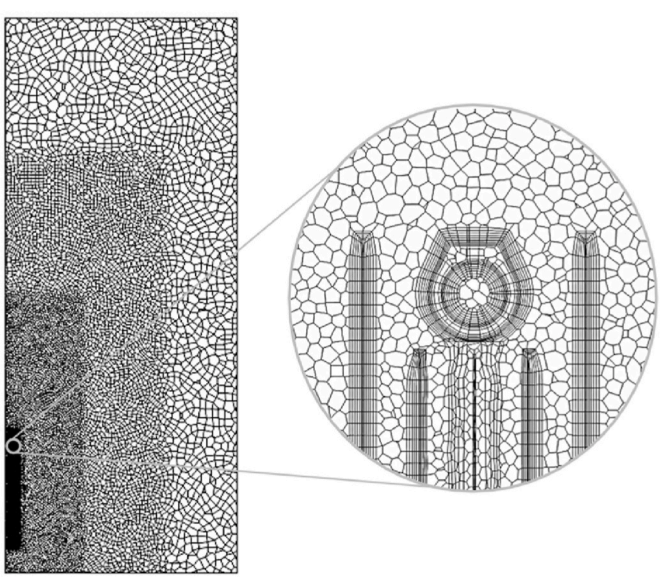

Fig. 6. Mesh with 18 M cells at XZ Plane and detail in radiator surface.

The average values for the inlet and outlet water temperature parameters (T_i, T_o) were also determined and are documented in Table 2. These parameters exhibit nearly constant evolutions throughout the measurement period. The mean standard deviation for T_i is 0.40 °C, indicating minimal variation in the inlet water temperature. Similarly, the mean standard deviation for T_o is 0.36 °C, suggesting consistent outlet water temperature values. The stability and low variability of these parameters indicate a nearly constant heat transfer process within the installation. Despite the initial transient nature of the process, after some time, approximately 8 h in this installation, thermal stability conditions are observed.

The five scenarios exhibit distinct characteristics in terms of room air temperature (T_r) and excess temperature of radiators (ΔT), according to the information summarized in Table 2. In Scenario 64/58 °C, the T_r is the lowest among all the scenarios, while the ΔT is the second highest. On the other hand, Scenario 67/41 °C is characterized by an intermediate ΔT and the second lowest T_r. Moving to Scenario 73/68 °C, it stands out with the highest ΔT and the second highest T_r. In contrast, Scenario 50/35 °C showcases the highest T_r and the second lowest ΔT. Finally, Scenario 50/35 °C distinguishes itself with the lowest ΔT and an intermediate T_r. These variations in T_r and ΔT across the different scenarios allow this study to cover different operational ranges of the installation.

Concerning the velocity and temperature parameters at the periphery of the radiators, a total of 84 points were monitored for each of the five scenarios being studied. Fig. 8 presents the corresponding measurements, with a distinction made for the 4 horizontal planes based on their height in meters (H1-blue (2.203 m); H2-cyan (2.383 m); H3-yellow (2.563 m); H4-red (2.743 m)), as depicted in Fig. 2 and described in Section 3.2.2. After analyzing Fig. 8, is evident that scenarios 64/58 °C, 67/41 °C and 73/68 °C exhibit a higher range of velocities and temperatures in the different planes compared to scenarios 50/35 °C and 39/29 °C. This outcome was as anticipated, given that these three scenarios involve a higher water inlet temperature and the three largest excess temperature of radiators above indoor air temperature (ΔT).

In addition, when examining plans H1 to H4, the closest plan to the radiator (H1-blue) consistently records the highest temperatures across all cases, except for the 73/68 °C scenario, which exhibits the greatest temperature variation. Furthermore, this scenario also displays the widest range of velocity and temperature variations within the plan, likely attributed to the effects resulting from the proximity to the radiator and the presence of radiator wall brackets. Regarding the H4 plan (Red), farthest from the radiator and closest to the beam, the smallest range of temperature and velocity variation was observed, attributed to the effect of the beam causing the airflow to circumvent the area.

Considering the observed influence of physical elements on Plans H1 and H4, an analysis of velocity and temperature evolutions was conducted for Plans H2 and H3 to investigate the impact of the radiators' serial positioning. The temperature and velocity profiles are presented in Fig. 9. As observed, the velocity distribution varies along the longitudinal planes (L1-L7), and it was also found that the measurements between the two radiators exhibit variations, with average velocity differences below 0.1 m/s and average temperature differences below 1 °C. These results lead to the conclusion that in parallel radiators, their temperature and velocity profiles are asymmetrical, regarding to the midpoint between the two radiators. In all scenarios, it is noticeable that the highest values of temperature and velocity are observed at point 17, which corresponds to the central location of the radiator nearest to the

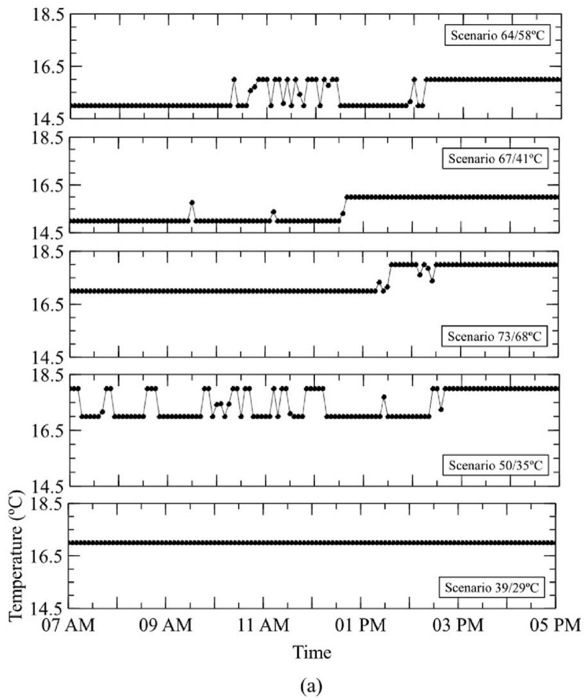

Fig. 7. Temperature evolutions for each measurement scenario: (a) room air (T_r) and (b) inlet and outlet water (T_i, T_o). The measurements for each scenario were completed in a single day and for scenarios (T_i/ T_o), see Table 2.

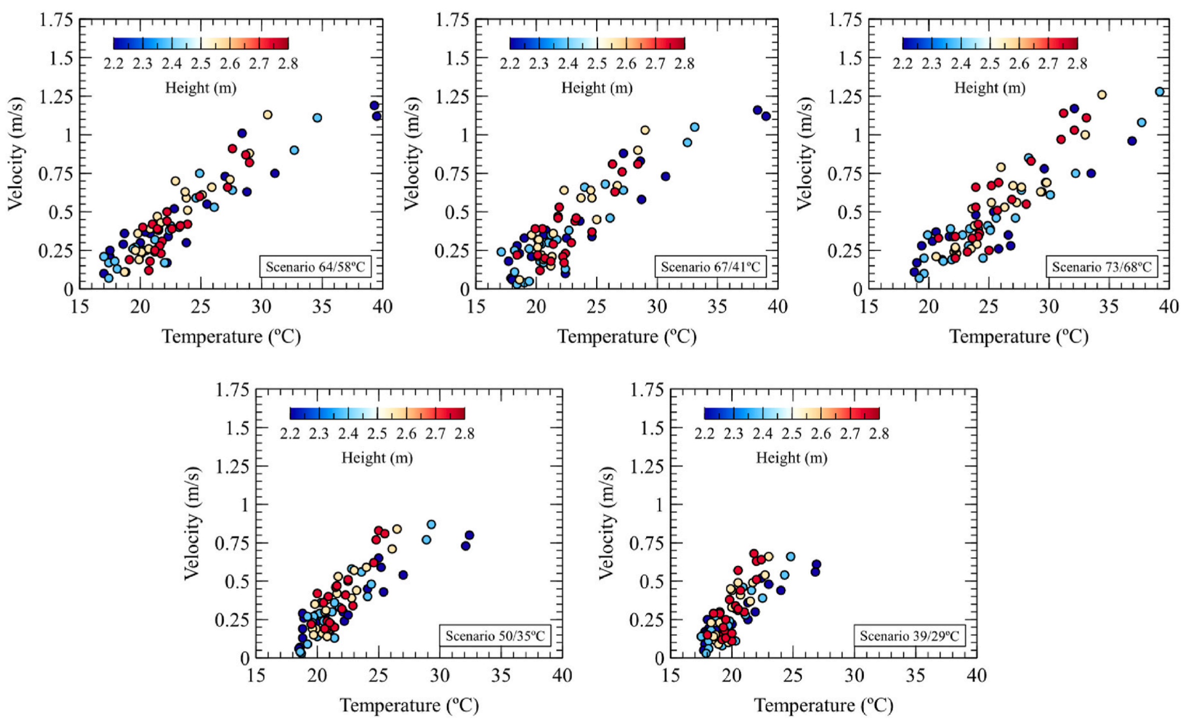

Fig. 8. Measurements of velocity and temperature at the periphery of the radiators for each measurement scenario. For scenarios (T_i/ T_o), see Table 2.

entry point of the hot water circuit.

Regarding the vertical planes (V1–V3), the presence of the room's beam geometry was found to impact the development of the thermal plume and the temperature distribution of the panel, which directly influences the velocity distribution and values, as previously observed in the study by Calisir et al., 2016 [27]. It can be observed that the velocity distribution is not symmetrical when considering the midpoint between the outer fins of a radiator element. This is due to the non-symmetrical temperature distribution on both sides of the panel radiator. One side of the panel faces the wall, while the other side faces the room. Consequently, due to the non-symmetrical temperature distribution, the velocity develops asymmetrically. Comparing the experimental data points resulting from the intersection of the H4 plane with the vertical planes V1 and V3, a lower velocity is observed in the plane closer to the beam (V1) compared to the more distant plane (V3) where the plume evolves. This velocity difference is approximately 0.3 m/s for scenarios (T_i/T_o)

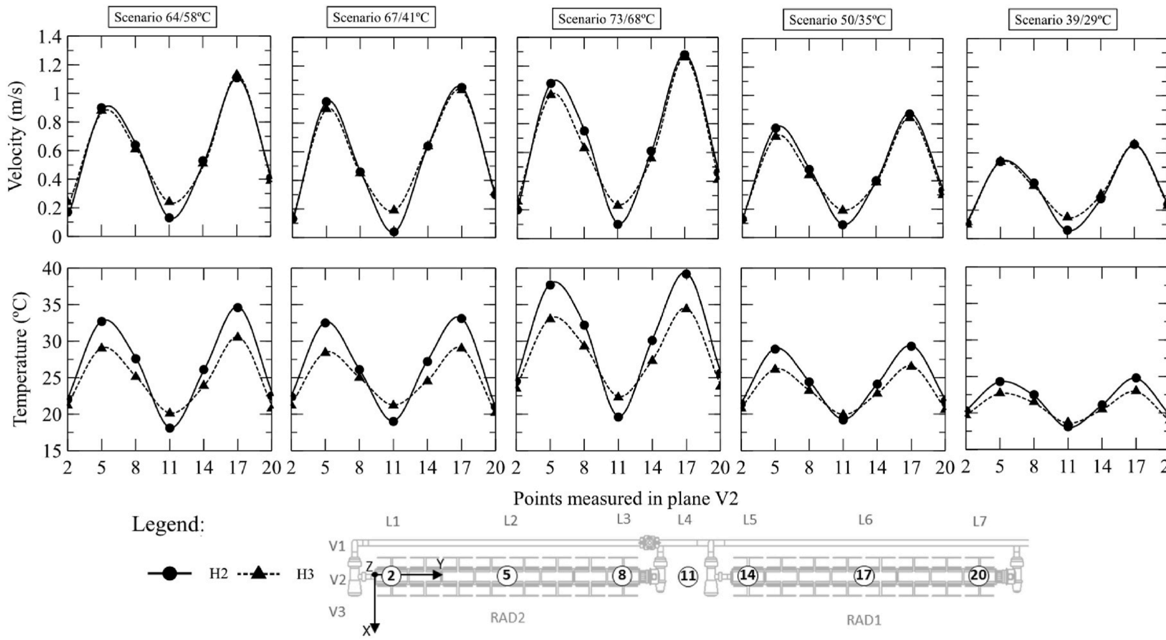

Fig. 9. Temperature and velocity profiles for the H2 and H3 planes along the measurement points of the V2 plane. For scenarios (T_i/ T_o), see Table 2, and for points measured, see Fig. 2.

64/58 °C, 73/68 °C, and 50/35 °C, and around 0.2 m/s for scenarios 67/41 °C and 39/29 °C.

The average velocity and temperature values for the H1–H4 have been determined based on the date in Annex A and will be used for validating the numerical model.

In the analysis of surface temperature, three cases were considered, with the number of measured points varying from 4 to 16 points for Cases I to III, respectively (Fig. 3). For all three cases, the average surface temperatures were determined as shown in Table 5, based on the data from Table A. 1 in Appendix A. To assess the similarity of surface temperatures between the two radiators, the difference between their average surface temperatures was calculated for each Case and scenario. This difference ranged from 0 °C to 1.4 °C, with Scenario (50/35 °C)/ Case I showing the minimum value and Scenario (67/41 °C)/Case II exhibiting the maximum value, indicating identical temperatures for both radiators. This is further supported by the similar temperature distribution observed in each of the five studied scenarios (Table 3), as indicated by the color gradient in Table A. 1 of Appendix A.

To compare the measurements of the three cases (I to III) and assess the influence of the number of points used to determine the average surface temperature, a relative error was calculated using Case III as a reference. The relative error varied between 0 % and 2.4 %, with Scenario 64/58 °C showing the minimum value and Scenario 50/35 °C displaying the maximum value.

The consistent occurrence of these very low errors across all five scenarios demonstrates that, for future experimental studies, measurements can be performed with only 4 points to obtain a reliable estimate of the average surface temperature of the radiator.

Table 5
Average surface temperature of the radiators in each of the Cases I to III.

Scenarios (T_i/ T_o)	Case I		Case II		Case III	
	RAD 1	RAD 2	RAD 1	RAD 2	RAD 1	RAD 2
64/58°C	49.4	49.8	49.5	49.6	49.4	48.8
67/41°C	45.1	43.9	45.2	43.8	44.4	43.6
73/68°C	56.9	57.4	57.3	57.2	57.5	56.2
50/35°C	36.3	36.3	36.3	36.1	36.0	35.5
50/35°C	29.8	29.5	30.1	29.5	29.6	28.9

4.2. CFD

In the CFD methodology, simulations convergence was ensured by controlling the residuals and monitoring the surface temperature of the radiators/porous media and the heat output. While there is no standardized method for evaluating convergence, all simulations showed a progressive decrease in residuals and reached a plateau, indicating convergence.

Specifically, the unsteady-state model with a time step of 0.01 s was employed to achieve a significant drop in the residuals by 3–5 orders of magnitude.

As explained in section 3.2, the CFD methodology (Fig. 4 consists of two steps. The first step plays a crucial role in determining the simplified numerical model used in the second step. In the second step, direct comparisons are made between the results obtained and the experimental results presented in Section 4.1. The experimental values used in the comparison are average values determined under experimental conditions in which the installation has already reached thermal equilibrium. These values help account for any measurement errors that may occur, yet they correspond to the same conditions as the numerical values. It is important to note that these results not only include the outlet temperature and heat transfer rate but also feature the average values of velocities and temperatures in the experimentally analysed planes, differentiating this study from most cases in the literature that only compare the outlet temperature and heat transfer rate.

In the process, first, the resistance coefficients were determined. To accomplish this, it was conducted six simulations using the 1/2-Element Model, covering a range of temperature and water inlet flow rates. Specifically, it was selected temperature values of 75, 55, and 35 °C, along with flow rates of 0.1, 0.5, and 1.2 m^3/h. To calculate the resistance coefficients, it was plotted the numerically obtained points on a curve described by Equation (17). In this study, it was focused solely on the properties in the darker region shown in Fig. 10-a, neglecting the top effects of the radiator's top geometry.

The results for each combined temperature and flow rate variant are depicted in Fig. 10-b. By fitting the data and considering an air density of 1.2068 kg/m^3 and viscosity of 1.86×10^{-5} Pa-s, it was obtained an inertial coefficient (K_i) of 2.34239 and a viscous coefficient (K_v) of 5.7×10^{-4} for this specific radiator type within the established operating

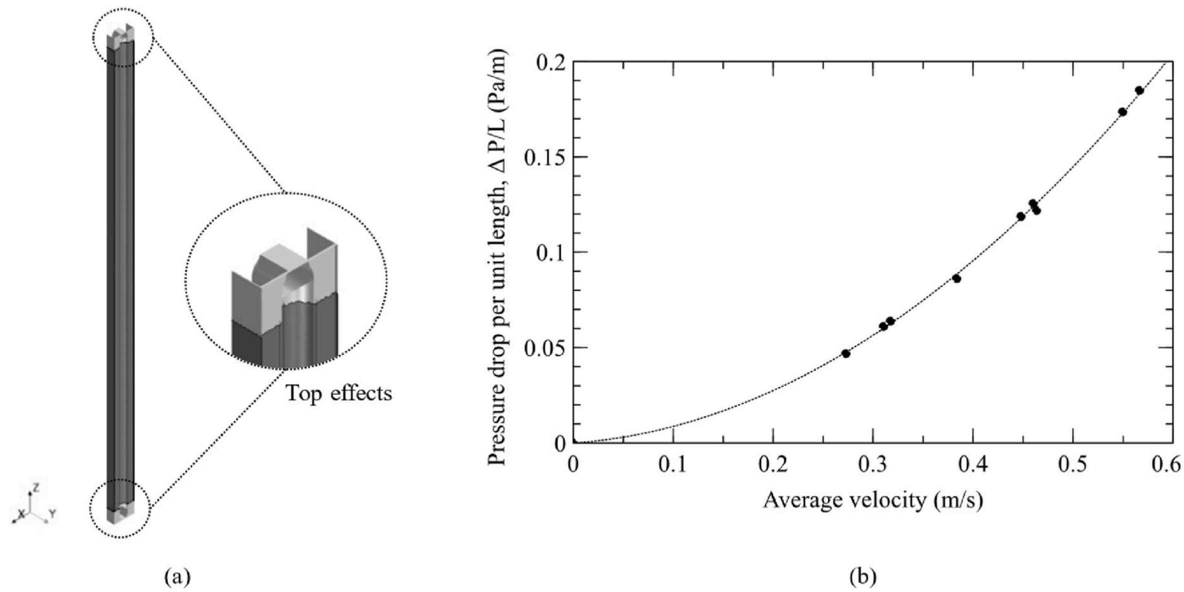

Fig. 10. Data for determination of resistance coefficients of the porous media: a) Simplification of top effects, and b) Pressure drop per unit length ($\Delta P/\ L$) as a function of average velocity.

range.

The higher value of the inertial coefficient compared to the viscous coefficient suggests that the flow resistance caused by the geometry and density of the porous media outweighs the resistance resulting from fluid viscosity. This phenomenon can be attributed to the low density of the porous media which was characterized by a porosity of 0.75 in this study, determined using Equation (12).

In summary, the findings indicate that the flow resistance primarily originates from the porous media's characteristics and density, rather than the fluid viscosity. These insights highlight the influence of the porous media on the overall flow behaviour in the radiator system under investigation.

Based on the results of the six simulations, the heat transfer coefficient (h) is determined using the expression provided in Equation (19). The results are presented in Table 6. To determine the heat transfer coefficient for the five experimental scenarios presented in Table 2, linear interpolation of the results is performed. For the scenarios ($T_i/\ T_o$) 64/58 °C, 67/41 °C, 73/68 °C, 50/35 °C, and 39/29 °C, the heat transfer coefficients obtained were 8.82, 10.30, 9.23, 9.49, and 8.77 W/m^{2}K, respectively.

Through the simulation using the 1-Element Model, it was determined the radiator's equivalent conductivity (k_{eq}). This determination was necessary because the radiator was modelled as a porous media in the shape of a parallelepiped, deviating from its original geometry. In this porous media model, anisotropic conductivity of the solid phase is accounted, with heat flow predominantly occurring in the x-direction for radiators. By applying Equation 18, it was obtained the value of 15.28 W/mK for k_{eq}, specifically for this direction, while maintaining the original conductivity of the radiator material in the other directions.

Furthermore, it was calculated the interaction area density for this radiator type, which amounts to 494.6/m. This density represents the ratio of the solid element's surface area to its total volume.

Table 6
Heat transfer coefficient for radiators (W/m^{2}K).

Flow (m^3/h)	Temperature (°C)		
	75	55	35
1.2	9.3	8.3	6.9
0.5	9.4	8.4	7.1
0.1	10.7	9.8	8.5

After the determination of parameters K_v, K_i, h and k_{eq}, Step 2 is implemented, which corresponds to the simplified model. However, to understand the potential application of this model in terms of computational effort and time, we compare it to the Detailed Model, which encompasses three physical aspects: solid, liquid, and gas. The Detailed Model, with its complexity and vast scale of approximately 18 million cells and incorporating radiation effects, required over 240 h of computation time using six processors. However, the simulation model showed remarkable agreement with experimental data for outlet water temperature (T_o) and output heat transfer rate (Q). The outlet temperature exhibited a consistent relative error below 5 % for all T_i/T_o scenarios, indicating precise predictions. Similarly, the relative error for heat transfer rates remained below 10 % for all scenarios, demonstrating accurate forecasting.

To reduce computation time, the radiator geometry was simplified by representing it as a porous media, reducing mesh elements by 83 % and computation time to less than 70 h on six processors. Additionally, the interior temperature profile was simplified using Equation (20), streamlining calculations by eliminating the need to model the detailed temperature distribution and water circuit. This approach aimed to optimize computational resources, ensuring a balanced cost-to-quality ratio, especially when applying the model to spaces with significant air masses. It is important to emphasize that in the simplified model, especially when porous media is employed, there might be some variations in the heat exchange calculations. Therefore, it is crucial to validate the parameter of heat transfer rate.

The results presented in Table 7, focusing on the relative errors between simulation and experimental data (base data in Table A. 2 of Annex A), showcase a robust agreement between the Simplified Model and experimental findings, particularly regarding the output heat transfer rate (Q). Relative errors in simulated heat transfer rates consistently stay below 8 % across all T_i/T_o scenarios. Notably, the scenario with a temperature difference of 39/29 °C demonstrates the most accurate prediction, while the highest relative error is observed in the 67/41 °C scenario.

Additionally, upon analysing the average velocities and temperatures in the H1–H4 planes (Fig. 2), it's evident that the discrepancies between the Simplified Model and the experimental data are mostly within acceptable bounds. The sole scenario showing relative errors exceeding 10 % is observed in the 73/68 °C scenario, whereas the rest of the scenarios demonstrate relative errors below 10 %. These results

Table 7
Relative error comparison between Simplified Model and experimental data for average velocity and temperature (H1–H4 planes) and surface temperature (Cases I-III). For scenarios (T_i/T_o) see Table 2, points measured see Fig. 2, and Cases I-II see Fig. 3.

Scenarios (T_i/T_o)	Q (W)	Velocity (m/s)				Temperature (ºC)				Surface Temperature (ºC)					
										Rad1			Rad2		
		Plane								Case					
		H1	H2	H3	H4	H1	H2	H3	H4	I	II	III	I	II	III
64/58ºC	5	-8	3	2	10	7	4	9	10	9	8	3	9	8	4
67/41ºC	8	-10	-4	-3	8	7	1	5	8	2	1	-1	5	4	1
73/68ºC	6	-7	-3	-6	-7	14	5	8	14	8	6	0	7	7	2
50/35ºC	5	-4	-7	-7	-9	5	1	3	6	4	3	1	4	4	3
50/35ºC	-4	8	10	9	4	1	-1	2	4	6	5	4	7	7	6

Legend: Green –|RE (%) | ≤ 10.5; Yellow – 10.5 < |RE (%) | ≤ 20.5; Red – |RE (%) | > 20.5.

underscore the overall reliability and effectiveness of the Simplified Model in accurately capturing the heat transfer characteristics within the system.

Comparison of individual radiator surface temperatures across scenarios reveals relative errors below 9 %, with errors below 5 % observed in the 67/41 °C and 50/35 °C scenarios. However, investigation into the influence of point quantity on average surface temperature determination (Case I to III - Fig. 3) shows relative error variations ranging from 1 % to 9 %. To enhance numerical model accuracy, it is recommended to employ 16 points (Case III) for average surface temperature determination, mitigating potential errors and bolstering temperature measurement reliability.

In a more qualitative analysis of the thermal plume evolution, it was examined the distribution of temperature and velocity in both the YZ plane (Fig. 11-a and Fig. 11-b, respectively) and the XZ plane (Fig. 12-a and Fig. 12-b, respectively) at the midpoint of the radiator farthest from the hot water inlet (Rad 2 - Fig. 2-b). By studying these distributions, it was able to further confirm the earlier findings regarding the asymmetry of the profiles in both the longitudinal (x) and transverse (y) directions across all scenarios.

These findings highlight the non-uniformity and asymmetry of the thermal plume development in both the YZ and XZ planes. This asymmetry can be attributed to various factors, including the positioning of the heat source, the radiator geometry, and the natural convection patterns within the space.

Overall, the numerical results showed a maximum error of 14 %

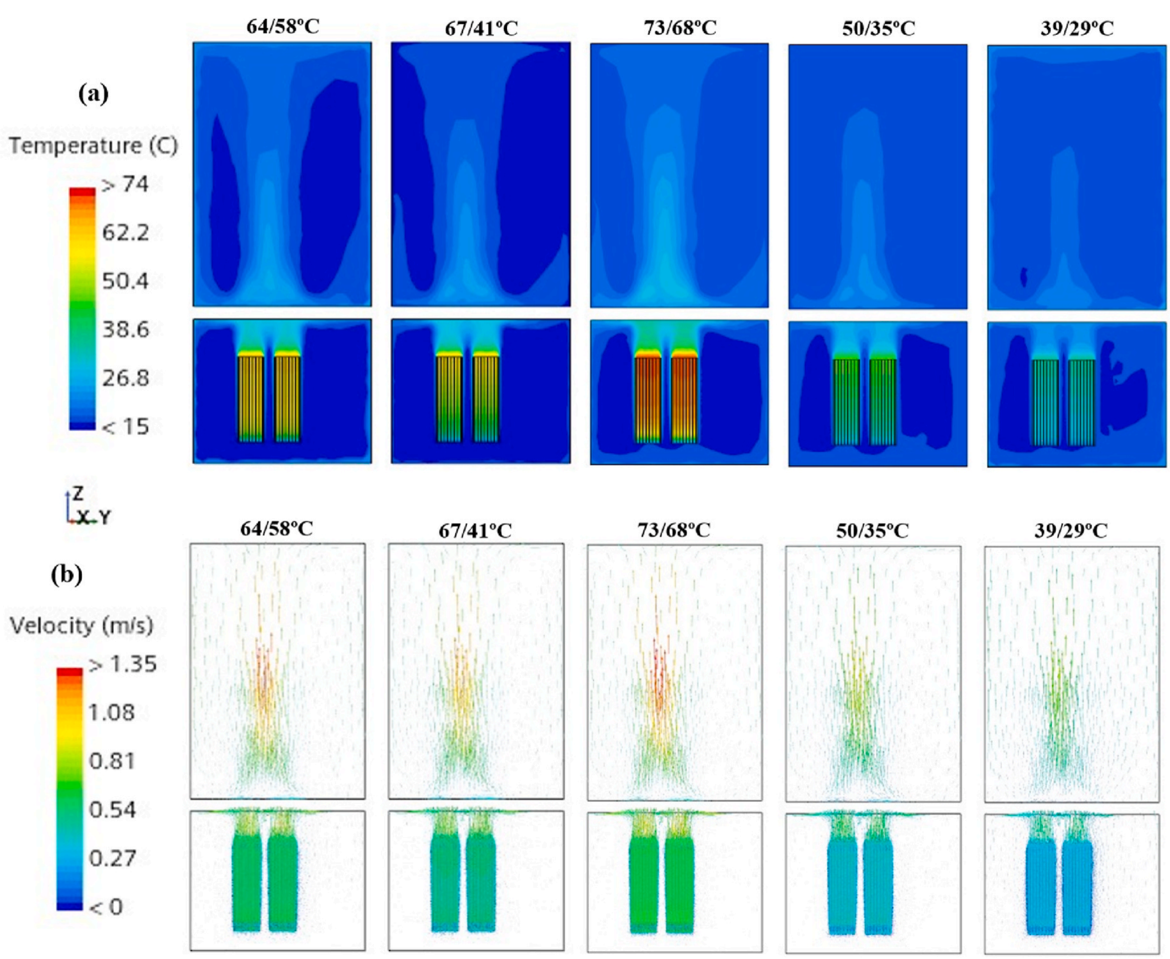

Fig. 11. Distribution in the YZ plane: (a) temperature and (b) velocity for Simplified Model.

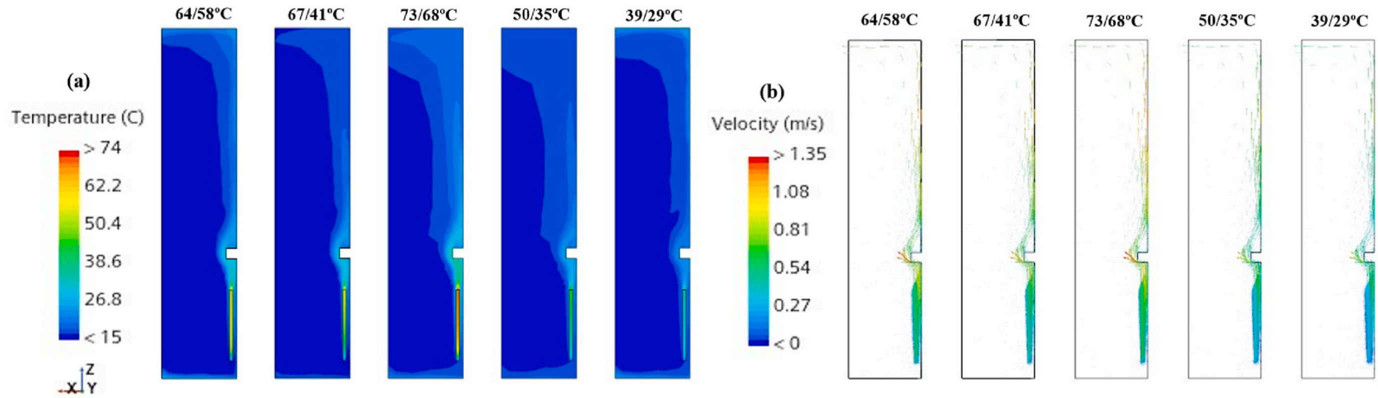

Fig. 12. Distribution in the XZ plane: (a) temperature and (b) velocity for Simplified Model.

when compared to the experimental data. It is important to highlight that these cases involved local parameters, which were subject to uncertainties in the experimental setup, complex turbulent/buoyant/heat transfer flows, and local oscillations or asymmetries. Despite these challenges, the agreement between the Simplified Model and the experimental data underscores the suitability and efficiency of the simplified approach in predicting the output heat transfer rate. Therefore, the proposed CFD methodology with the use of a Simplified Model emerges as a practical and computationally efficient alternative to be applied in spaces with large masses of air and without controlled environmental conditions.

Certainly, every research effort possesses its natural limitations. In this specific study, experimental results were presented for a particular type of radiator with a specific geometry. Although the experimental methodology can be adapted for various radiator types, the conclusions drawn from this study must be understood within this limited context. Additionally, restrictions in the size of the CFD domain, due to the presence of fixed chambers on the periphery for other tests, must also be considered. These limitations impacted the scale of the model concerning the total volume of the testing room, potentially influencing certain aspects of the analyses. Nevertheless, it's crucial to emphasize that these specific limitations do not diminish the validity of the findings presented in this study.

Looking forward, it's worth noting that this methodology holds the potential for expansion into different porous medium configurations. Considering future extensions, researchers could explore diverse radiator types and contemplate the removal or adaptation of the fixed chambers. By doing so, a more comprehensive analysis of thermal interactions in varied volumes could be achieved. This expansion not only enhances the model's robustness but also broadens the applicability and significance of the findings across a wider range of practical scenarios.

5. Conclusions

In this study, it was successfully developed and validated a simplified CFD model for predicting the development of thermal plumes in spaces with large masses of air and without controlled environmental conditions. The model was validated using experimental data obtained from a full-scale model, ensuring its accuracy and reliability.

The experimental measurements conducted under steady-state conditions revealed nearly constant evolutions for the inlet and outlet water temperatures, with average standard deviations of 0.40 °C for T_i and 0.36 °C for T_o. These findings indicate a stable and consistent heat transfer process within the installation, providing reliable data for future validation studies and further investigations. The study encompassed a wide range of scenarios with different variations of T_i/T_o, including 64/58 °C, 67/41 °C, 73/68 °C, 50/35 °C, and 39/29 °C, and monitored additional parameters such as velocity and temperature at the periphery of the radiators. The analysis revealed that the higher T_i/T_o scenarios exhibited a wider range of velocities and temperatures across different planes compared to the lower T_i/T_o scenarios. Furthermore, the study demonstrated that radiators in a parallel configuration exhibit asymmetrical temperature and velocity profiles relative to the midpoint between them. The surface temperature measurements of the radiators exhibited a consistent distribution. In addition, the reliable estimates of the average surface temperature can be obtained with just 4 measurement points (Case I - Fig. 3), as the errors varied only between 0 % and 2.4 %.

The results obtained from the Simplified Model in the CFD simulations (Table 7), which incorporates a porous media, have demonstrated the effectiveness of the proposed CFD methodology (Fig. 4). The comparison of parameters such as outlet temperature, heat transfer rate, and velocity and temperature evolutions (Table 7) revealed relative errors below 10 %, except for the specific scenario 73/68 °C, where higher relative errors were observed in only two temperature evolutions. Notably, the velocity in all planes showed average values below 10 %, indicating reliable predictions of thermal plume development using the simplified model. However, when determining the surface temperature of the radiators, it is advisable to use Case III (Fig. 3), which involves 16 measurement points for more accurate results. Nevertheless, the application of Case I, with only 4 points, is also viable since the errors in relation to the experimental data are below 10 % for all cases. Overall, the numerical results showed a maximum error of 14 % when compared to the experimental data.

Furthermore, a qualitative analysis was conducted to examine the distribution of temperature and velocity in the YZ and XZ planes at the midpoint of the radiator farthest from the hot water inlet (Figs. 10 and 11). The results confirmed the asymmetrical nature of the profiles in both the longitudinal and transverse directions across all scenarios, indicating non-uniform and asymmetrical development of the thermal plumes. These findings provide indications of a possible influence of factors such as the location of heat sources, radiator geometry, and patterns of natural convection in shaping the asymmetric behaviour of thermal plumes in the analysed space, given that the profiles are asymmetric but exhibit different forms compared to results from studies where radiator geometry and location differ [27]. However, it is important to note that this study encompasses only one type of radiator, under fixed location conditions, albeit with variable ambient conditions.

It is important to highlight that the computational times of the Simplified Model, in comparison to the Detailed Model, decreased from approximately 240 h to around 70 h, on six processors.

Regarding limitations, this study has the limitation that the experimental results were confined to a specific radiator type and geometry. However, it is important to note that a full-scale model was employed, and measurements were conducted in-situ for different operational and environmental scenarios, thereby enhancing the model's reliability.

Acknowledging the restricted CFD domain due to fixed peripheral chambers, it is crucial to emphasize that these limitations do not undermine the overall validity of the study. Despite these limitations, the significant potential of applying the CFD methodology to other types of heat sources and conditions stands out, emphasizing the need for validation to ensure their reliability.

The developed CFD methodology provides a simplified model that serves as a valuable resource for designers and engineers aiming to improve natural ventilation systems in various construction projects. This includes both new constructions and renovations of large spaces with heat sources, such as atriums, sports complexes, industrial pavilions, spas, and pools. The application of the simplified model allows for the study of multiple solutions with minimal computational demands. It predicts the development of thermal plumes, considering their influence on the proper air distribution within spaces, ensuring energy efficiency and occupant comfort. The insights gained from this study are essential references for future research and practical applications in natural ventilation design across diverse architectural projects.

CRediT authorship contribution statement

Rafaela Mateus: Writing – original draft, Validation, Software, Methodology, Investigation, Formal analysis, Data curation, Conceptualization. **Armando Pinto:** Writing – review & editing, Supervision, Resources, Methodology, Funding acquisition, Formal analysis, Conceptualization. **José M.C. Pereira:** Writing – review & editing, Supervision, Resources, Methodology, Funding acquisition, Formal analysis, Conceptualization.

Declaration of competing interest

The authors declare that they have no known competing financial interests or personal relationships that could have appeared to influence the work reported in this paper.

Data availability

No data was used for the research described in the article.

Acknowledgements

The authors acknowledge Fundação para a Ciência e a Tecnologia (FCT) for its financial support via the project LAETA Base Funding (DOI: 10.54499/UIDB/50022/2020).

Appendix A

Appendix A contains the experimental results used to calculate the average values and relative errors presented in Section 4.2.

Table A. 1
Experimental results of the surface temperature of the radiators in each of the Cases I to III.

Scenarios (T_i/T_o)		Case I				Case II				Case III							
		RAD 1		RAD 2		RAD 1		RAD 2		RAD 1				RAD 2			
64/58ºC	Points	51.1	51.3	52.0	51.9	52.4	52.4	52.7	52.7	57.0	57.7	57.2	54.9	55.7	55.7	57.8	53.6
		47.8	47.5	47.7	47.8	49.5	49.3	50.1	50.1	48.7	50.7	51.1	49.4	48.4	50.7	51.1	49.3
						47.0	46.6	45.7	46.6	47.1	49.1	48.9	47.4	46.4	48.7	49.2	47.2
										41.5	43.8	43.9	43.0	40.4	42.5	43.0	41.5
67/41ºC	Points	49.9	49.3	48.5	48.9	51.7	51.3	50.8	50.0	56.4	55.2	54.5	52.2	56.2	55.4	55.0	53.1
		40.5	40.7	38.8	39.5	45.6	45.3	43.8	44.1	47.1	48.3	48.4	46.5	45.9	47.1	47.7	46.0
						38.3	38.8	36.5	37.4	40.9	42.3	42.6	41.5	39.3	40.7	41.4	40.5
										32.8	33.7	34.3	34.1	31.1	32.3	32.8	32.5
73/68ºC	Points	59.1	59.4	59.6	59.9	60.4	60.9	60.2	60.8	65.6	64.9	64.0	64.1	64.3	62.9	64.5	64.2
		54.6	54.6	54.9	55.1	57.0	57.3	57.4	57.8	56.2	59.1	60.3	57.7	54.7	57.2	58.4	58.3
						53.8	54.1	53.1	53.8	53.9	56.7	58.4	58.0	52.6	55.2	55.8	56.5
										47.5	50.6	51.8	51.4	46.9	49.1	49.1	50.0
50/35ºC	Points	39.3	38.9	39.7	39.5	40.5	40.0	40.8	40.9	43.5	42.6	42.5	41.8	43.4	43.1	42.8	41.6
		33.5	33.7	32.7	33.3	36.7	36.2	36.1	36.2	37.2	38.5	38.4	36.9	36.9	38.1	37.9	37.3
						32.2	32.4	31.0	31.6	33.4	34.6	34.6	34.0	32.5	33.6	34.3	33.8
										28.6	29.4	29.7	29.5	27.6	28.0	28.3	28.2
	AVG.	**36.3**		**36.3**		**36.3**		**36.1**		**36.0**				**35.5**			
39/29ºC	Points	31.8	31.6	31.3	31.4	32.6	32.7	32.5	32.5	34.6	34.1	33.5	33.4	34.6	33.5	34.0	33.0
		28.0	28.0	27.4	27.9	30.5	30.6	29.2	29.7	30.5	31.4	31.3	30.3	29.7	30.1	31.1	29.8
						27.2	27.2	26.0	26.8	27.9	28.8	29.0	28.4	27.1	27.6	27.7	27.5
										24.7	25.4	25.6	25.4	23.6	23.9	24.7	24.3
Legend:		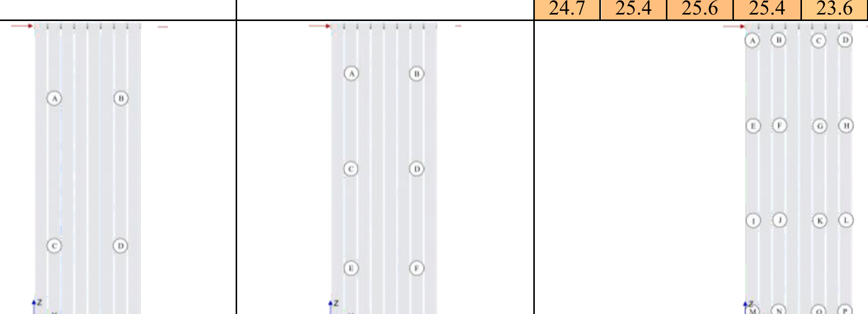															
		Progressive color scale: Purple for higher temperatures, pink or orange for intermediate temperatures, and yellow for cooler temperatures.															

Table A. 2
Experimental results of the average velocity and temperature Values for H1–H4 planes and surface temperature for Cases I-III.
Legend: SM – Simplified Model; RE – Relative Error; Green –|RE (%) | ≤ 10.5; Yellow – 10.5 < |RE (%) | ≤ 20.5; Red – |RE (%) | > 20.5.

Scenarios (T_i/T_o)		T_o (ºC)	Q (W)	Velocity (m/s)				Temperature (ºC)				Surface Temperature (ºC)					
												Rad1			Rad2		
				Plane								Case					
				H1	H2	H3	H4	H1	H2	H3	H4	I	II	III	I	II	III
64/58ºC	Experimental	58.7	4651.4	0.48	0.40	0.47	0.43	23.8	22.6	22.5	23.0	49.4	49.5	49.4	49.8	49.6	48.8
	SM	-	4886.8	0.44	0.41	0.48	0.47	25.4	23.4	24.5	25.2	54.0	53.5	50.7	54.1	53.5	50.7
	RE (%)	-	5	-8	3	2	10	7	4	9	10	9	8	3	9	8	4
67/41ºC	Experimental	41.4	3696.7	0.43	0.36	0.42	0.39	23.6	22.5	22.3	22.6	45.1	45.2	44.4	43.9	43.8	43.6
	SM	-	3980.2	0.39	0.35	0.41	0.42	25.3	22.6	23.4	24.5	45.9	45.7	43.8	45.9	45.7	43.9
	RE (%)	-	8	-10	-4	-3	8	7	1	5	8	2	1	-1	5	4	1
73/68ºC	Experimental	68.6	5800.8	0.54	0.46	0.53	0.58	27.1	25.7	25.7	25.9	56.9	57.3	57.5	57.4	57.2	56.2
	SM	-	6123.6	0.50	0.45	0.50	0.53	30.9	26.9	27.7	29.5	61.5	60.9	57.5	61.6	61.0	57.6
	RE (%)	-	6	-7	-3	-6	-7	14	5	8	14	8	6	0	7	7	2
50/35ºC	Experimental	34.6	2126.4	0.35	0.33	0.37	0.40	22.5	21.8	21.6	21.9	36.3	36.3	36.0	36.3	36.1	35.5
	SM	-	2228.0	0.33	0.31	0.35	0.36	23.6	22.0	22.3	23.2	37.7	37.6	36.4	37.7	37.6	36.4
	RE (%)	-	5	-4	-7	-7	-9	5	1	3	6	4	3	1	4	4	3
39/29ºC	Experimental	29.1	1279.9	0.27	0.25	0.29	0.33	20.6	20.0	19.9	20.1	29.8	30.1	29.6	29.5	29.5	28.9
	SM	-	1230.7	0.30	0.28	0.32	0.34	20.7	19.8	20.3	21.0	31.6	31.5	30.7	31.6	31.5	30.7
	RE (%)	-	-4	8	10	9	4	1	-1	2	4	6	5	4	7	7	6

References

[1] R.C. Adhikari, M. Pahlevani, Characteristics of thermal plume from an array of rectangular straight fins with openings on the base in natural convection, Int. J. Therm. Sci. 182 (2022) 107798, https://doi.org/10.1016/j.ijthermalsci.2022.107798.

[2] D. Etheridge, A perspective on fifty years of natural ventilation research, Build. Environ. 91 (2015) 51–60, https://doi.org/10.1016/j.buildenv.2015.02.033.

[3] G. Carrilho da Graça, P. Linden, Ten questions about natural ventilation of non-domestic buildings, Build. Environ. 107 (2016) 263–273, https://doi.org/10.1016/j.buildenv.2016.08.007.

[4] World Green Building Council, Every Building on the Planet Must Be 'net Zero Carbon' by 2050 to Keep Global Warming below 2°C – New Report, 2023 ccessed Febr. 2023.

[5] European Commission, Climate Change and You, 2023. Accessed Febr. 2023.

[6] European Commission, Can You Afford to Heat Your Home?, 2021. Accessed Febr. 2023.

[7] M. Pinto, F.M. da Silva, J. Viegas, V.P. de Freitas, Sistemas de Ventilação Natural em Edifícios de Habitação . Requisitos para a sua Modelização, in: Int. Conf. Eng. UBI2011 - Innov. Dev, 2011.

[8] A. Pinto, R. Mateus, J. Silva, M. Lopes, NZEB modular prefabricated building system, Sustain. Autom. Smart Constr. - Springer (2021), https://doi.org/10.1007/978-3-030-35533-3_20.

[9] T. Calisir, H.O. Yazar, S. Baskaya, Thermal performance of PCCP panel radiators for different convector dimensions – an experimental and numerical study, Int. J. Therm. Sci. 137 (2019) 375–387, https://doi.org/10.1016/j.ijthermalsci.2018.12.007.

[10] A.R. Rahmati, A. Gheibi, Experimental and numerical analysis of a modified hot water radiator with improved performance, Int. J. Therm. Sci. 149 (2020), https://doi.org/10.1016/j.ijthermalsci.2019.106175.

[11] E. Aydar, I. Ekmekçi, Thermal efficiency estimation of the panel type radiators with CFD analysis, Isi Bilim. Ve Tek. Dergisi/J. Therm. Sci. Technol. 32 (2012) 63–71.

[12] Q. Wu, Z. Wang, J. Dong, J. Liu, A method for judging the overheating of the radiator in the compensation of window downdraught based on thermal image velocimetry, Build. Environ. 197 (2021), https://doi.org/10.1016/j.buildenv.2021.107858.

[13] J.A. Myhren, S. Holmberg, Improving the thermal performance of ventilation radiators e The role of internal convection fins, Int. J. Therm. Sci. 50 (2011) 115–123, https://doi.org/10.1016/j.ijthermalsci.2010.10.011.

[14] S.M.B. Beck, S.C. Grinsted, S.G. Blakey, K. Worden, A novel design for panel radiators, Appl. Therm. Eng. 24 (2004) 1291–1300, https://doi.org/10.1016/j.applthermaleng.2003.11.026.

[15] T. Calisir, H.O. Yazar, S. Baskaya, Evaluation of flow field over panel radiators to investigate the effect of different convector geometries, J. Build. Eng. 33 (2021), https://doi.org/10.1016/j.jobe.2020.101600.

[16] T. Calisir, S. Baskaya, The influence of different geometrical dimensions of convectors on the heat transfer from panel radiators, SN Appl. Sci. 3 (2021) 1–16, https://doi.org/10.1007/s42452-021-04276-2.

[17] İ. Ekmekci, E. Aydar, A new design for panel radiators using CFD, Conf. Adv. Mech. Eng. ISTANBUL 2016 – ICAME2016 (2016).

[18] M. Embaye, S. Mahmoud, Thermal performance of hydronic radiator with fl ow pulsation e Numerical investigation, Appl. Therm. Eng. 80 (2015) 109–117, https://doi.org/10.1016/j.applthermaleng.2014.12.056.

[19] V. Chandak, S.B. Paramane, W.V. d Veken, J. Codde, Numerical investigation to study effect of radiation on thermal performance of radiator for onan cooling configuration of transformer, IOP Conf. Ser. Mater. Sci. Eng. Pap 88 (2015), https://doi.org/10.1088/1757-899X/88/1/012033.

[20] M. Embaye, S. Mahmoud, Numerical evaluation of indoor thermal comfort and energy saving by operating the heating panel radiator at different flow strategies, Energy Build. 121 (2016) 298–308, https://doi.org/10.1016/j.enbuild.2015.12.042.

[21] T. Calisir, H.O. Yazar, S. Baskaya, Determination of the effects of different inlet-outlet locations and temperatures on PCCP panel radiator heat transfer and fluid flow characteristics, Int. J. Therm. Sci. 121 (2017) 322–335, https://doi.org/10.1016/j.ijthermalsci.2017.07.026.

[22] A. Jahanbin, E. Zanchini, Effects of position and temperature-gradient direction on the performance of a thin plane radiator, Appl. Therm. Eng. 105 (2016) 467–473, https://doi.org/10.1016/j.applthermaleng.2016.03.018.

[23] R. Marchesi, F. Rinaldi, C. Tarini, F. Arpino, G. Cortellessa, M. Dell'isola, G. Ficco, Experimental analysis of radiators' thermal output for heat accounting, Therm. Sci. 23 (2019) 989–1002, https://doi.org/10.2298/TSCI170301168M.

[24] K. Võsa, A. Ferrantelli, T. Mall, J. Kurnitski, Experimental Analysis of Emission Efficiency of Parallel and Serial Connected Radiators in EN442 Test Chamber, vol. 132, 2018, pp. 531–544, https://doi.org/10.1016/j.applthermaleng.2017.12.109.

[25] G.A. Ganesh, S. Lata, T. Nath, Numerical simulation for optimization of the indoor environment of an occupied office building using double-panel and ventilation radiator, J. Build. Eng. 29 (2020) 101139, https://doi.org/10.1016/j.jobe.2019.101139.

[26] D. Brandl, T. Mach, R. Heimrath, H. Edtmayer, C. Hochenauer, Thermal evaluation of a component heating system for a monastery cell with measurements and CFD simulations, J. Build. Eng. 39 (2021) 102264, https://doi.org/10.1016/j.jobe.2021.102264.

[27] T. Calisir, S. Baskaya, H.O. Yazar, S. Yucedag, Experimental and numerical prediction of flow field around a panel radiator, Conf. Environ. Renew. Energy 5 (2016).

[28] Y. Wang, A. Sergent, D. Saury, D. Lemonnier, P. Joubert, Numerical study of an unsteady confined thermal plume under the influence of gas radiation, Int. J. Therm. Sci. 156 (2020), https://doi.org/10.1016/j.ijthermalsci.2020.106474.

[29] M. Gomes, Avaliação das Taxas de Infiltração de Ar no Sector Residencial, MSc Thesis - Univ. Coimbra, 2013.

[30] J.S. Turner, J.S. Turner, Buoyancy Effects in Fluids, Cambridge university press, 1979.

[31] R.H. Hernández, Natural convection in thermal plumes emerging from a single heat source, Int. J. Therm. Sci. 98 (2015) 81–89, https://doi.org/10.1016/j.ijthermalsci.2015.06.010.

[32] Y.N. Lyakhov, Experimental investigation of free convection above a heated horizontal wire, J. Appl. Mech. Tech. Phys. 11 (1970) 355–359, https://doi.org/10.1007/BF00908122.

[33] K. Urakawa, I. Morioka, M. Kiyota, Swaying motion of the buoyant plume above a horizontal line heat source, Proc. 1st ASME-JSME Therm. Engng Conf., Honolulu. 3 (1983) 215–220.

[34] D. Han, T. Zhang, Y. Qin, Y. Tan, Experimental study on thermal plume characteristics of building façades based on PIV technology, Sustain. Cities Soc. 77 (2022) 103589, https://doi.org/10.1016/j.scs.2021.103589.
[35] R.J.M. Bastiaans, C.C.M. Rindt, F.T.M. Nieuwstadt, A.A. Van Steenhoven, Direct and large-eddy simulation of the transition of two- and three-dimensional plane plumes in a confined enclosure, Int. J. Heat Mass Tran. 43 (2000) 2375–2393, https://doi.org/10.1016/S0017-9310(99)00302-6.
[36] V.T. Vishnu, A.K. De, P.K. Mishra, Statistics of thermal plumes and dissipation rates in turbulent Rayleigh-Bénard convection in a cubic cell, Int. J. Heat Mass Tran. 182 (2022) 121995, https://doi.org/10.1016/j.ijheatmasstransfer.2021.121995.
[37] T.-A. Nguyen, N. Kakuta, Experimental study on initial thermal plumes from small heating parts in water, Exp. Therm. Fluid Sci. 142 (2022) 110803, https://doi.org/10.1016/j.expthermflusci.2022.110803.
[38] G. Chanakya, P. Kumar, Effects of diffuse and collimated beam radiation on plume formation in natural convection within a cubical enclosure, Int. J. Heat Mass Tran. 188 (2022) 122558, https://doi.org/10.1016/j.ijheatmasstransfer.2022.122558.
[39] A. Bangian-Tabrizi, X. Zhang, Y. Jaluria, Solution to inverse natural convection problem using experimental data, Int. J. Heat Mass Tran. 189 (2022) 122721, https://doi.org/10.1016/j.ijheatmasstransfer.2022.122721.
[40] Z. Liu, D. Yin, Y. Niu, G. Cao, H. Liu, L. Wang, Effect of human thermal plume and ventilation interaction on bacteria-carrying particles diffusion in operating room microenvironment, Energy Build. 254 (2022) 111573, https://doi.org/10.1016/j.enbuild.2021.111573.
[41] S.C. Wong, S.H. Chu, Revisit on natural convection from vertical isothermal plate arrays–effects of extra plume buoyancy, Int. J. Therm. Sci. 120 (2017) 263–272, https://doi.org/10.1016/j.ijthermalsci.2017.06.018.
[42] S.C. Wong, S.H. Chu, M.H. Ai, Revisit on natural convection from vertical isothermal plate arrays II—3-D plume buoyancy effects, Int. J. Therm. Sci. 126 (2018) 205–217, https://doi.org/10.1016/j.ijthermalsci.2018.01.008.
[43] X. Gao, A. Li, C. Yang, Study on natural ventilation driven by a restricted turbulent buoyant plume in an enclosure, Energy Build. 177 (2018) 173–183, https://doi.org/10.1016/j.enbuild.2018.07.048.
[44] A. Teskeredzic, R. Blazevic, Transient radiator room heating — mathematical model and solution algorithm, Buildings 8 (2018), https://doi.org/10.3390/buildings8110163.
[45] R. Mateus, J.M.C. Pereira, A. Pinto, Natural ventilation of large air masses : experimental and numerical techniques review, Energy Build. (2023) 113120, https://doi.org/10.1016/j.enbuild.2023.113120.
[46] D. Risberg, M. Risberg, L. Westerlund, CFD modelling of radiators in buildings with user-defined wall functions, Appl. Therm. Eng. J. 94 (2016) 266–273, https://doi.org/10.1016/j.applthermaleng.2015.10.134.
[47] Z. Cao, H. Sun, T. Niu, X. Lu, A simplified method of radiator to improve the simulation speed of room temperature distribution, Li, Y., Zhu, Q., Qiao, F., Fan, Z., Chen, Y. Adv. Simul. Process Model. ISSPM 2020, Adv. Intell. Syst. Comput. 1305 (2021), https://doi.org/10.1007/978-981-33-4575-1_38.
[48] EN 442-2, EN 442-2, Radiators and Convectors – Part 2: Test Methods and Rating, Com. Eur. Norm., 2015.
[49] R.S. John, R. Howell, M. Pinar Mengüc, Kyle Daun, Thermal Radiation Heat Transfer, 7.a ed., CRC Press, Boca Raton, 2020 https://doi.org/10.1201/9780429327308.
[50] Y. Cengel, M. Boles, M. Kanoglu, Thermodynamics - an Engineering Approach, 9.a ed., McGraw-Hill Education, New York, 2019.
[51] A. Pinto, Ventilação Das Termas Romanas De Chaves - Estudo de estratégias de ventilação e de aquecimento, Lisboa LNEC, relatório n.º 293/2018 - Dep. Edifícios/NAICI, 2018.
[52] SIEMENS, Simcenter STAR-CCM+ Documentation - Version 2020.2, SIEMENS, 2020.
[53] N. Padoin, A.T.O.D. Toé, C. Soares, CFD Applied to the Investigation of Flow Resistances in Porous Media, Congr. Interam, Comput. Apl. a la Ind. Procesos, 2014.
[54] O.O. Noah, J.F. Slabber, J.P. Meyer, CFD simulation of natural convection heat transfer from heated micro- spheres and bottom plate in packed beds contained in slender cylindrical geometries, Int. Conf. Porous Media (2014) 1–13.
[55] Thermoworks, emissivity table, thermoworks. https://www.thermoworks.com/emissivity-table/, 2023.
[56] MatWeb, aluminum 3003-H12, December 2022, https://www.matweb.com/search/DataSheet.aspx?MatGUID=5b30b87291e84c5e843a9b0025b7dfc6, 2022.

Nomenclature

A: Area [m^2]
h:: Water enthalpy [J/kg] or convective coefficient [W/m^2 °C]
H: Height of radiator [m]
k:: Turbulence kinetic energy or heat conduction coefficient [W/m.K]
K_v:: Viscous resistance coefficient [−]
K_i:: Inertial resistance coefficient [−]
L:: length of radiator [m]
$\dot{m}$:: Water mass flow rate [kg/s]
n: Exponent [−]
P: Power [W] or Pressure [Pa]
Q: Heat output of radiator [W]
$\dot{Q}$ :: Water flow rate [m^3/h]
T: temperature [°C]
V: Volume [m^3]
x, y, z:: Coordinates [−]

Greek Symbols

σ: Stefan–Boltzmann constant [W/m^2 K^4]
ε:: Dissipation rate of turbulent kinetic energy [m^2/s^3]
μ:: Dynamic viscosity [kg/m.s]
ξ:: Emissivity [−]
ρ:: Density [kg/m^3]
χ:: Porosity [−]

Subscripts

i: inlet
o: outlet
r: room
s: surface
w: wall
f: fluid